This document is downloaded from DR-NTU (https://dr.ntu.edu.sg)
Nanyang Technological University, Singapore.

Strong plasmon–exciton interactions on nanoantenna array–monolayer WS2 hybrid system

Liu, Lin; Tobing, Landobasa Yosef Mario; Yu, Xuechao; Tong, Jinchao; Qiang, Bo; Fernández-Domínguez, Antonio I.; Garcia-Vidal, Francisco J.; Zhang, Dao Hua; Wang, Qijie; Luo, Yu

2020

Liu, L., Tobing, L. Y. M., Yu, X., Tong, J., Qiang, B., Fernández-Domínguez, A. I., . . . Luo, Y. (2020). Strong plasmon–exciton interactions on nanoantenna array–monolayer WS2 hybrid system. Advanced Optical Materials, 8(5), 1901002-. doi:10.1002/adom.201901002

https://hdl.handle.net/10356/138664

https://doi.org/10.1002/adom.201901002

© 2019 WILEY-VCH Verlag GmbH & Co. KGaA, Weinheim. All rights reserved. This paper was published in Advanced Optical Materials and is made available with permission of WILEY-VCH Verlag GmbH & Co. KGaA, Weinheim.

Downloaded on 27 Aug 2022 21:57:32 SGT

Strong Plasmon-Exciton Interactions on Nanoantenna Array-Monolayer WS_2 Hybrid System

Lin Liu[1,‡], Landobasa Y.M. Tobing[1,‡], Xuechao Yu[1], Jinchao Tong[1], Bo Qiang[1], Francisco J. Garcia-Vidal[2,3], Dao Hua Zhang[1,*], Qi Jie Wang[1,*], and Yu Luo[1,*]

[1]School of Electrical & Electronic Engineering, Nanyang Technological University, Singapore, 639798.

[2]Departamento de Física Teorica de la Materia Condensada and Condensed Matter Physics Center (IFIMAC), Universidad´ Autonoma de Madrid, 28049 Madrid, Spain.

[3]Donostia International Physics Center (DIPC), Donostia/San Sebastian, Spain.

[‡]These authors contributed equally to this work.
[*]Correspondence should be addressed to YL (luoyu@ntu.edu.sg), QJW (qjwang@ntu.edu.sg) , DHZ (edhzhang@ntu.edu.sg).

Abstract: Strong plasmon-exciton interactions in monolayer transition-metal-dichalcogenides (TMDCs) is crucial for applications in light emissions, nonlinear optics and quantum communications, and their realizations require highly localized electric fields parallel to the transition dipole moment of the quantum emitters. Here, we present a systematic study of light-matter interaction in planar dimer nanoantenna of nanoscale gaps coupled with monolayer WS_2, where the effects of the local field enhancement and spatial mode overlap in the plasmon-exciton coupling strength are experimentally investigated. Importantly, we demonstrate anti-crossing behaviors in the strong coupling regime with a Rabi splitting of $\Omega = 118\ meV$ for gold bowtie antenna with 7 nm gap, and $\Omega = 138\ meV$ for gold dimer arrays 10 nm gap.

Keywords: Strong coupling, localized surface plasmons, WS_2, polariton, photoluminescence

The interaction of highly localized modes with nanoscale emitters has gained much attention in the past decades[1–3] for its importance in fundamental quantum physics, such as Bose- Einstein condensation[4–7], quantum vortex[8] and non-Hermitian physics[9,10] and applications in optical transistors[11,12], polariton switches[13,14] and single photon sources[15]. Based on the energy exchange rate between matter and electromagnetic modes relative to their respective damping constants, light-matter interaction strength can be classified into weak and strong coupling regimes. In a weakly-coupled system, optical processes involving light and matter are irreversible, exemplified in spontaneous emissions of quantum emitters [16–19]. However, this is qualitatively different when the light-matter interaction enters the strong coupling regime, where coherent oscillations of energy between excitons and photons dominates over the electromagnetic damping, manifesting in clear spectral splitting known as the Rabi splitting [20–23]. Realization of strong coupling requires a large density of photonic states, which is mainly dependent on the spatiotemporal confinement of electromagnetic fields characterized by the mode volume V and resonance Q-factor, $LDOS \propto Q/V$. For this, many efforts have been devoted to realize photonic microcavities with high Q/V, namely, high-Q resonances based on photonic crystals[24–26] and whispering gallery modes [27]. Despite their ultrahigh Q resonances, realizations of strong coupling in these platforms often require their characterizations implemented in cryogenic temperatures due to the mismatch between the photon and exciton lifetimes. In addition, light-matter coupling occurs within an interaction volume dictated by the diffraction-limit, thereby hindering the characterization of light-matter interaction at a single molecule level. Alternatively, plasmonic systems have been explored for strong light-matter interaction at the nanoscale, particularly because plasmonic nanocavities also exhibit high Q/V due to their strong field confinement at the deep subwavelength scale despite their much lower Q-factor than their dielectric counterparts. Different kinds of quantum emitters have been explored for studying strong coupling with plasmonic nanostructures, including J-aggregates[28–32], dye molecules[33–35] and quantum dots[36,37]. Recently, monolayers made of transition metal dichalcogenides (TMDs), when combined with plasmonic nanostructures, have been shown to be excellent platforms for achieving strong coupling at room temperature due to their direct bandgap and strong binding energy of their excitons. [38,39]

Different kinds of plasmonic systems have been explored for plasmon-exciton coupling with TMDs, including nanocavities, [40] self-assembled metallic nanoparticles, [41–44] nanoantenna arrays, [17,45–47] and metal nanohole arrays. [48] For strong coupling, it is important to design plasmonic nanocavities with a mode field parallel to the transition dipole moment of the excitons in TMDs. In nanoparticle on mirror (NPoM) systems [40], for example, multilayered TMDs are used such that the transition dipole moment of the TMDs is reoriented towards the out-of-plane resonance mode field. However, for monolayer TMD in which the transition dipole moment is purely in-

plane, the plasmonic mode of the NPoM system only couples weakly to the exciton despite its strong field enhancement in the dielectric spacer separating the nanoparticle and the metal film, which is largely due to its orthogonal mode field. In the context of synthesized nanoparticles, attempts to reduce misalignment between the mode field and the exciton transition dipole have been explored, notably in the use of gold bi-pyramid [43] and ultrathin gold nanodisks [44].

Meanwhile, top-down fabricated planar nanoantennae with nanogaps exhibit strong in-plane mode fields, and have been demonstrated to couple strongly with quantum emitters [49–51]. The main advantage of the top-down fabricated antennae lies in their lithographic flexibility, which could be used as a platform for studying light-matter interaction with TMD, for example in the moderate coupling of bowtie nanoantenna with monolayer MoS_2 that manifests in the emergence of Fano resonances [17]. In this work, we present an in-depth analysis of the strong-coupling anti-crossing characteristics in planar gold nanoantenna with nanogaps, namely bowtie and square dimer nanoantennae. By fabricating nanoantennae of different gaps, sizes, and periodicity on the same chip, we are able to investigate systematically the roles of *E*-field enhancements and spatial mode overlap in the coupling strength. By introducing ultrathin dielectric interlayer, we observe the effect of spatial mode overlap where ~20-30% decrease of Rabi splitting is observed when 2 nm thick Al_2O_3 layer is inserted. Specifically, we experimentally demonstrate a direct evidence for the correlation between the local density of states and the coupling strength. We demonstrate a Rabi splitting of $\Omega = 138\ meV$ based on square dimer of sub-10 nm gaps, which is shown to be in strong-coupling regime and confirmed by photoluminescence measurements of TMD-dimer systems based on CVD-grown and exfoliated monolayer WS_2.

Theoretical model

The strong coupling of a plasmonic resonance with excitons supported by a monolayer TMD can be understood from the so-called Jaynes-Cummings (JC) Hamiltonian, which describes the interaction of electromagnetic field with a two-level atom [52,53]

$$\widehat{H}_{JC} = \hbar\omega_{pl}\hat{a}^{\dagger}\hat{a} + \hbar\omega_0\hat{\sigma}_z/2 + \hbar g_c(\hat{a}\hat{\sigma}_+ + \hat{a}^{\dagger}\hat{\sigma}_-), \tag{1}$$

where the first term describes the electromagnetic energy characterized by the plasmon mode frequency ω_{pl}, the second term describes the two-level excitation characterized by exciton frequency ω_0, and the third term describes the exciton-photon interaction characterized by coupling strength g_c. $\hat{a}^{\dagger}$ and $\hat{a}$ is the creation and annihilation operators for the photon, while $\hat{\sigma}_+$ and $\hat{\sigma}_-$ are the raising and lowering operators for the exciton. $\hat{\sigma}_z$ is the atomic inversion operator. Rearranging the JC Hamiltonian into an eigenvalue problem for the hybrid states gives

$$\begin{pmatrix} \omega_{pl} + i\hbar\gamma_{pl}/2 & g_c \\ g_c & \omega_0 + i\hbar\gamma_0/2 \end{pmatrix}\begin{pmatrix}\alpha\\ \beta\end{pmatrix} = \omega_{\pm}\begin{pmatrix}\alpha\\ \beta\end{pmatrix}, \tag{2}$$

where (α, β) are eigen coefficients satisfying $|\alpha|^2 + |\beta|^2 = 1$, and

$$\omega_{\pm} = \frac{1}{2}\left(\omega_{pl} + \omega_0 + i\frac{\gamma_{pl}-\gamma_0}{2}\right) \pm \frac{1}{2}\sqrt{\left(\omega_{pl} - \omega_0 + i\frac{\gamma_{pl}-\gamma_0}{2}\right)^2 + 4g_c^2} \tag{3}$$

are the eigenfrequencies $\omega_{\pm}$ of the hybrid modes, with γ_{pl} and γ_0 as the dissipation rates of uncoupled plasmon and exciton modes. By ignoring the dissipation terms, the eigenfrequencies can be simplified as [54,55]

$$\omega_{\pm} = \frac{1}{2}(\omega_{pl} + \omega_0) \pm \sqrt{g_c^2 + \delta^2/4}, \tag{4}$$

with $\delta = \omega_{pl} - \omega_0$ as the detuning between plasmon mode and exciton energy. The vacuum Rabi splitting is the resonance splitting at zero detuning, $\Omega = 2g_c$, which can be derived from Eq. 4 as $\Omega = \sqrt{(\omega_+ - \omega_0)(\omega_0 - \omega_-)}$. The system is said to be in strong coupling when the rate of energy exchange is faster than the loss. The rather generic criterion for strong coupling is $\Omega > (\gamma_+ + \gamma_-)/2$, where $\gamma_{\pm}$ are the linewidths of the split resonances. A more rigorous criterion for the strong coupling has been studied in detail, [56] suggesting that strong coupling is achieved when $|\Omega/(\gamma_{pl} - \gamma_0)| > 1$. For *N* excitons coupled with a plasmon mode, the coupling strength can be written as: $g_c = \sqrt{N}\mu_e|E_{cav}|$, where is μ_e the transition diople moment of exciton, $|E_{vac}| = \sqrt{\hbar\omega/2\epsilon\epsilon_0 V}$ is the vaccuum field. Quality factor can be calculated from $Q = \omega_{pl}/\gamma_{pl}$. Therefore, strong plasmon-exciton coupling is related with LDOS as $g_c/\gamma_{pl} \sim Q\sqrt{N/V}$.

Results and discussions

As shown in Fig. 1, we present a detailed study of plasmon-exciton coupling of gold nanoantenna arrays lithographically fabricated on monolayer WS_2 films deposited on SiO_2/Si substrates, where square dimer and bowtie antenna designs were chosen in this study for their strong local *E*-fields across nanogaps and their small mode volume. As commented above, the advantage of these top-down fabricated antennae over self-assembled nanoparticle on metal (NPoM) systems lies in their in-plane local *E*-fields that aligns with the transition dipole moment of the monolayer WS_2. Furthermore, the lithographic flexibility of the top-down fabrication allows us to tune the antenna dimensions for studying plasmon-exciton coupling at different resonance detuning. We also introduced an ultrathin dielectric spacer between the WS_2 and gold nanoantenna for investigating the effect of the plasmon mode spatial overlap with the WS_2 to the plasmon-exciton coupling strength. The scanning electron micrographs (SEM) of the fabricated gold nanostructures are shown in Fig. 1c (bowtie nanoantenna) and Fig. 1d (square dimer). In order to ensure a small mode volume, we fabricated these nanoantenna with gap spacing (g) in ~10 nm range (see Methods). The other parameters such as the side length (s) and apex angle (θ) were chosen to match the plasmon mode frequency (ω_{pl}) close to the WS_2 exciton transition (ω_0). The periodicities (P_x, P_y) of the nanoantenna array were designed as $P_x = P_y = 4s$ to minimize the near-field coupling between nanoantennae, which is known to impart resonance broadening and, consequently, decreases the Q factor. This is confirmed in our numerical simulations which reveals that the scattering cross sections (σ_{scat}) of the nanoantenna are smaller than the unit cell area $(\sigma_{scat} < P_x P_y)$. However, the far-field coupling still exists among these nanoantenna due to the strong radiation of the dimer antenna. We used this far-field coupling to further enhance the local *E*-fields, from which our numerical simulation show that the *E*-field can be ~2.5x higher in a nanoantenna array (with $P_{x,y} = 4s$) than in an isolated antenna. Another purpose of using the nanoantenna array is to investigate the mode interaction under two mode excitations. The first type is the normal excitation (in bright field geometry), which generates a Fano-like resonance that results from the interaction between the localized surface plasmon (LSP) of the gold nanoantenna and the thin film resonance of the 295 nm thick SiO_2 film. The second type is the oblique excitation (in dark field geometry) which generates only the LSP modes.

The WS_2 considered in this work was grown by chemical vapor deposition (CVD) instead of realized by mechanical exfoliation. Despite the lower optical quality of the former, we note the importance of the large-scale uniformity of the WS_2 film in this study, particularly in the context of characterizing plasmon-exciton couplings with gold nanoantenna arrays fabricated across the sample. For transition metal dichalcogenide (MX_2) layered compounds (M = Mo, W and X = S, Se, Te), there are generally four Raman-active modes, namely the A_{1g}, E_{1g}, E^1_{2g} and E^2_{2g} modes [57]. In order to investigate the monolayer properties of the CVD-grown WS_2, we focus our attention to the in-plane vibrational E^1_{2g} mode and the out-of-plane vibrational A_{1g} mode, where the former shows little dependence on the film thickness and the latter undergoes a blue shift with increasing layer number [58]. As shown in Fig. 1e, Raman characterization of the CVD-grown WS_2 shows the E^1_{2g} mode at 353 cm^{-1} and A_{1g} mode 417 cm^{-1} with a 64.1 cm^{-1} frequency difference between the two modes. This value is close to the 65.5cm-1 frequency difference for monolayer WS2 in other report[58], thereby confirming the monolayer characteristics of our CVD-grown WS_2. The photoluminescence of our CVD-grown WS_2 (under 532 nm laser excitation) is presented in Fig. 1f, showing exciton peak at $\omega_0 = 2eV$ with $\gamma_0 = 25meV$ linewidth. We also note the two small peaks near the 532 nm excitation, which are the two Raman signals in Fig. 1e.

The mappings of the optical response of the gold nanoantenna arrays were carried out by hyperspectral imaging system (see methods) schematically illustrated in the supporting information (Fig. S1). Figure 2a displays the *x*-polarized scattering spectrum (in the bright-field geometry) of square dimer arrays coupled with monolayer WS_2 with near zero detuning $(s = 60nm, g = 20nm)$, where a weak dip is observed near the exciton transition in between more pronounced resonance dips. The weak dip signifies the mode splitting which results from the plasmon-exciton coupling, with the split modes indicated by the weak scattering peaks. Such an obscured spectral splitting is attributed to the hybrid mode resulting from the interference between the LSP mode of the nanoantenna and the mode arising from the multiple reflections inside the 295 nm SiO_2 film. In order to verify this, we excite the square dimers under oblique illumination (in the dark-field geometry), with the purpose of eliminating multiple reflections that builds up only under normal incidence. As evident in Fig. 2b, we observed an optical response with clear mode splitting at the exciton transition (denoted by the shaded band), indicating the absence of the Fabry-Perot (FP)-like mode under oblique excitation. The small bump around 546 nm is not associated with any

resonance as it is the spectral artifact of the mercury lamp itself. The hybridization of this mode is numerically simulated in Fig. 2c, which shows that the two dips at 500 nm and 700 nm stem from the modified FP resonance condition due to the presence of gold nanoantenna (dashed blue curve). The phase response (ϕ) of a strongly radiating plasmonic antenna such as dimer or disk is close to $\phi = \pi$ at LSP resonance (for negligible damping loss), translating to a rapid change of the FP interference condition from constructive to destructive, satisfying the FP resonance condition in two different frequencies. Thus, in addition to the LSP resonance position that remains unchanged, we observe two reflectance dips associated with light localization inside SiO_2 film. In the presence of monolayer WS_2, a mode splitting is to be expected for the reflection peak at the exciton transition (solid blue curve). The simulated spectra differ from the measure spectra notably in their spectral contrasts. Such a difference in spectral contrast is attributed to the nonideal mode excitation in our experiment, where the plasmonic nanoantenna arrays were excited at different incident angles dictated by the numerical aperture of our objective lens (which is NA = 0.55). Other factors include the permittivity of both the physically deposited gold and the CVD-grown WS_2 monolayer, and also the surface roughness and roundedness in the gold nanoantenna structure.

We present in Fig. 3 anti-crossing behaviors of gold bowtie and square dimer arrays coupled with monolayer WS_2 based on dark-field measurements. The upper (ω_+) and lower (ω_-) energy branches of the hybrid modes are plotted for different resonance detunings $(\delta = \omega_{pl} - \omega_0)$, realized through geometric variations of the nanoantenna. Red dashed line denotes the WS_2 exciton energy at 2 eV, while the blue and green solid curves denote the fitting based on Eq. 4. In Fig. 3a, we present the anti-crossing behavior for gold bowtie nanoantenna, which were fabricated with different nominal apex angles ($\theta = 40°, 50°, 60°$) and side lengths ($s = 60nm, 80nm, 100nm$). Although the gap spacing was nominally fixed as $g = 20nm$, the actual gap spacing in the fabricated structures can be tuned by adjusting the exposure dose and time. In our experiments, we have realized bowtie antenna with gaps as small as $g \sim 7nm$ with good repeatability. The Rabi splitting for WS_2-bowtie system was found to be $\Omega = 118meV$. In Fig. 3b, we present the anti-crossing behavior for gold square dimer, which were fabricated with different nominal side lengths ($s = 60nm, 80nm, 100nm$) and gap spacings ($g = 20nm, 30nm, 40nm$). Similar to bowtie structures, the real gap spacings were realized by tuning the exposure dose and develop time, from which gold square dimer with gap as small as $g \sim 10nm$ have been realized. The Rabi splitting for WS_2-dimer system was found to be $\Omega = 138meV$. It is worth noting that wider Rabi splitting is observed for the square dimers than for bowtie antennae despite the smaller mode volume of the latter, which indicates the higher Q/V values and therefore larger local density of states ($LDOS$) of the former. This is verified by the smaller local *E*-field of the bowtie antenna (Fig. 3e), as compared to that of the square dimer (Fig. 3f). The geometry shapes of the nanoantenna arrays were designed to have LSP resonances near WS_2 transition at 620 nm ($2eV$). The details of geometrical structures, resonance wavelength, Q factor and mode area for the two structures are given in Table. S1 (Supporting Information), showing that square dimer antenna exhibits 70% higher Q-factor with 26% larger mode area compared to those of the bowtie antenna. In terms of coupling ($g \propto \sqrt{Q/V}$) [59], this translates to 16% higher coupling strength ($g_{dimer}/g_{bowtie} = 1.16$). This is in excellent agreement with our experiments, where the ratio of the Rabi splitting gives $\Omega_{dimer}/\Omega_{bowtie} = 1.17$. The role of *E*-field enhancement in the coupling strength is studied in isolated square dimers separated by much larger periodicity ($P_{x,y} = 2\mu m$). In such situations, both the near-field and far-field couplings can be ignored, which results in 2.5x smaller *E*-field enhancements for the isolated square dimers (Fig. S3c-d). The much higher field enhancement in nanoantenna arrays is attributed to Rayleigh-Wood anomaly arising from the diffraction condition of the pattern. Periodic patterning of dimers into an array reduces the linewidth of the dimers LSP resonance [60,61]. The anti-crossing behavior for isolated square dimers is given in the supplementary information (Fig. S3b), showing narrower Rabi splitting ($\Omega = 114meV$) compared to that of the square dimer arrays ($\Omega = 138meV$).

We have also investigated the role of spatial overlap between the plasmon mode and the excitons in the coupling strength, where an ultrathin dielectric spacer is introduced between the gold nanoantenna array and monolayer WS_2. Insertion of 2 nm thick Al_2O_3 layer leads to a decrease of the Rabi splitting from $\Omega = 118meV$ to $\Omega = 94meV$ for the bowtie antenna (Fig. 3c), and from $\Omega = 138meV$ to $\Omega = 97meV$ for the square dimers (Fig. 3d). In addition to the decrease of spatial overlap and more light localization within the ultrathin film (Fig. S4), a decrease in the coupling strength is also caused by the increased proportion of the out-of-plane *E*-fields which does not couple with the in-plane transition dipole moment of the monolayer WS_2 excitons. The strong coupling regimes of our results are evaluated by the two criteria described briefly in the previous section. Using the square dimer represents the largest Rabi splitting in this work, where $\gamma_+ = 70.6meV$, $\gamma_- = 67.5meV$, $\gamma_0 = 64meV$,

$\gamma_{pl} = 247.8meV$, $\Omega = 138meV$, we found that $\Omega - (\gamma_+ + \gamma_-)/2 \cong 68.9meV$ and $|\Omega/(\gamma_{pl} - \gamma_0)| \cong 1.5$, indicating that our system satisfies strong coupling condition. In the presence of 2 nm Al_2O_3 film, where $\gamma_+ = 65.7meV$, $\gamma_- = 57.9$, $\Omega = 97meV$, we found that $\Omega - (\gamma_+ + \gamma_-)/2 \cong 27.95meV$ and $|\Omega/(\gamma_{pl} - \gamma_0)| \cong 1.05$. This suggests that our system is still in strong coupling region, albeit close to the boundary between weak and strong coupling.

Another fingerprints of the plasmon-exciton interaction can be found in the photoluminescence (PL) response of the monolayer WS_2 coupled with square dimers of $s = 80nm$ (blue) and $s = 100nm$ (green). Although the mode splitting associated with strong coupling can be clearly observed in the dark field scattering results, we observe no splitting in the PL response. However, we observed a red shift in the PL emissions accompanied with an increasing shoulder below 620 nm in the WS_2-dimer system (Fig. 4a). To further understand this, we plot the PL contribution from the dimer structure, $PL_{dimer} = PL_{dimer-WS2} - PL_{WS2}$, obtained by subtracting the PL response with that of the WS_2 film (Fig. 4a, red curve). As shown in Fig. 4b, we note that the spectral dip in the PL response coincides with that in the dark field spectra, with the higher energy mode emission (ω_+) much less pronounced than the lower energy emission (ω_-). We found that the splitting in the PL response is narrower than the dark field scattering counterparts, which appears to be in agreement with other works that investigated PL splitting in J-aggregates coupled to silver nanoprisms [62]. This is because the splitting in the absorption cross section is smaller than the splitting in the scattering cross section as plotted in the supplementary information (Fig. S6). The more pronounced PL peak in the PL splitting may have been caused by the quality of the monolayer WS_2 and the way it couples with the gold nanoantenna. We investigated this using mechanically exfoliated monolayer WS_2 transferred onto gold nanoantenna array (Fig. S5), and found that the PL response exhibits splitting but with more pronounced higher energy emission, contrary to what we observed in Fig. 4a. However, the detailed mechanisms for the more pronounced PL peaks remains unclear as there are still many factors influencing the PL response of a strongly coupled system [62,63].

Conclusion

Strong plasmon-exciton interaction in monolayer WS_2 coupled with gold nanoantenna arrays have been investigated. Bowtie and square dimer antenna of sub-10 nm gaps are employed in this study for their high Q/V property which stems from their strongly confined *E*-fields across nanogaps. We coupled the exciton with two different modes excited under bright field and dark field geometries, and characterize anti-crossing behavior with Rabi splitting as large as 138meV for gold square dimer arrays. The role of the *E*-field enhancement in the coupling strength is studied by eliminating the near-field and far-field couplings in the sparse nanoantenna arrays, which significantly decreases the local *E*-field, leading to narrower Rabi splitting. The role of the spatial mode overlap is investigated through inserting ultrathin dielectric spacers between nanoantenna and monolayer WS_2, where a 20-30% decrease in the coupling strength is observed when a 2 nm-thick Al_2O_3 spacer is introduced. Using the criteria for the strong coupling, the WS_2-dimer system is justified to be in the strong coupling region, even with a 2 nm dielectric spacer. This is mainly attributed to the fact that the in-plane transition dipole of the monolayer WS_2 aligns with the strong in-plane *E*-fields of the nanoantenna confined within nanoscale gaps. The signature of the strong coupling is also characterized in the PL measurements of our WS_2-dimer system, with a more pronounced lower energy emission. The cause for such asymmetrical PL splitting remains unclear, and future investigations are still needed to understand the PL splitting properties of strongly coupled system.

Methods

Sample Fabrication.

The full-area WS_2 was grown on 295nm thick thermal oxide on silicon substrate (from 2DSemiconductors Inc), with the monolayer thickness properties of the WS_2 confirmed by atomic force microscopy (AFM) and Raman spectroscopy. The emission wavelength of the CVD-grown and mechanically exfoliated WS_2 were characterized by micro-photoluminescence. The ultrathin 2 nm thick Al_2O_3 spacer layer for studying the near field coupling between plasmon and WS_2 was deposited by atomic layer deposition (Cambridge Nanotech). The gold dimer and bowtie nanoantenna arrays were fabricated by electron beam lithography (20 keV energy and 30 pA beam current), followed by sonicated cold development in a mixture of *n*-pentyl acetate and isopropanol at 6°C temperature; and 30 nm thick gold evaporation at 0.05 nm/s rate. The lift-off pattern transfer was then conducted in *n*-methyl pyrrolidone for 10 minutes, followed by isopropanol rinse.

Optical Characterization.

The samples were characterized in microscope setting coupled to hyperspectral imaging system. In the reflection measurements, mercury lamp (X-Cite 120) was focused onto the sample via 50x objective lens (NA = 0.55) under bright-field geometry. The signals were directed to the hyperspectral imaging system, while the piezo-controlled stage is scanned in order to obtain the reflection mapping. The reflectance is obtained by normalizing the reflection signals to the reflection of gold film of the same thickness. The scattering measurements followed the same routine but in dark-field geometry. The scattering is normalized to the scattered signals from the substrate. In all these measurements, polarizers were placed after the source and before the hyperspectral imaging system in order to eliminate polarization mixing. The micro-photoluminescence and Raman measurements were conducted by WITec system under confocal geometry, based on 532 nm laser focused by 100x objective lens (NA = 0.8). The grating was set as 600 g/mm (for PL measurement) and 1800 g/mm (for Raman measurement).

Numerical calculations.

The full-wave simulations were done by a commercial finite-difference time-domain software (FDTD Solutions, Lumerical Inc) based on normal planewave excitation and periodic boundary conditions in *x* and *y* directions. The permittivities of the gold, silicon, and Al_2O_3 were all taken from the software database, with the Johnson-Christy model adopted for the permittivity of gold. The monolayer WS_2 is modelled as a 0.618 nm thick dielectric layer, whose permittivity modelled as Lorentzian oscillator [64,65] $\epsilon(E) = 1 + \sum_{k=1}^{N} f_k/(E_k^2 - E^2 - i\gamma_k E)$. Here, f_k and γ_k are the oscillator strength and the linewidth of the *k*th oscillator; and E_k is the oscillation energy that runs over the full spectral range.

Reference

[1] K. Huang, *Proc. R. Soc. London. Ser. A. Math. Phys. Sci.* **1951**, *208*, 352.
[2] J. J. Hopfield, *Phys. Rev.* **1958**, *112*, 1555.
[3] Y. J. Chen, E. Burstein, D. L. Mills, *Phys. Rev. Lett.* **1975**, *34*, 1516.
[4] Y. Yamamoto, H. Deng, H. Haug, *Riv. del Nuovo Cim.* **2010**, *33*, 591.
[5] H. Deng, H. Haug, Y. Yamamoto, *Rev. Mod. Phys.* **2010**, *82*, 1489.
[6] H. Deng, G. Weihs, C. Santori, J. Bloch, Y. Yamamoto, *Science (80-.).* **2002**, *298*, 199.
[7] T. Byrnes, N. Y. Kim, Y. Yamamoto, *Nat. Phys.* **2014**, *10*, 803.
[8] L. Dominici, G. Dagvadorj, J. M. Fellows, D. Ballarini, M. De Giorgi, F. M. Marchetti, B. Piccirillo, L. Marrucci, A. Bramati, G. Gigli, M. H. Szymańska, D. Sanvitto, *Sci. Adv.* **2015**, *1*, e1500807.
[9] L. Chang, X. Jiang, S. Hua, C. Yang, J. Wen, L. Jiang, G. Li, G. Wang, M. Xiao, *Nat. Photonics* **2014**, *8*, 524.
[10] R. El-Ganainy, K. G. Makris, M. Khajavikhan, Z. H. Musslimani, S. Rotter, D. N. Christodoulides, *Nat. Phys.* **2018**, *14*, 11.
[11] D. Ballarini, M. De Giorgi, E. Cancellieri, R. Houdre, E. Giacobino, R. Cingolani, A. Bramati, G. Gigli, D. Sanvitto, *2013 Conf. Lasers Electro-Optics Eur. Int. Quantum Electron. Conf. CLEO/Europe-IQEC 2013* **2013**, DOI: 10.1109/CLEOE-IQEC.2013.6801821.
[12] A. V. Zasedatelev, A. V. Baranikov, D. Urbonas, F. Scafirimuto, U. Scherf, T. Stöferle, R. F. Mahrt, P. G. Lagoudakis, *Nat. Photonics* **2019**, *13*, DOI: 10.1038/s41566-019-0392-8.
[13] T. Gao, P. S. Eldridge, T. C. H. Liew, S. I. Tsintzos, G. Stavrinidis, G. Deligeorgis, Z. Hatzopoulos, P. G. Savvidis, *Phys. Rev. B - Condens. Matter Mater. Phys.* **2012**, *85*, 1.
[14] T. G. Tiecke, J. D. Thompson, N. P. De Leon, L. R. Liu, V. Vuletić, M. D. Lukin, *Nature* **2014**, *508*, 241.
[15] J. McKeever, A. Boca, A. D. Boozer, J. R. Buck, H. J. Kimble, **2003**, *425*, 3.
[16] D. G. Baranov, M. Wersäll, J. Cuadra, T. J. Antosiewicz, T. Shegai, *ACS Photonics* **2018**, *5*, 24.
[17] B. Lee, J. Park, G. H. Han, H. S. Ee, C. H. Naylor, W. Liu, A. T. C. Johnson, R. Agarwal, *Nano Lett.* **2015**, *15*, 3646.
[18] K. Børkje, A. Nunnenkamp, J. D. Teufel, S. M. Girvin, *Phys. Rev. Lett.* **2013**, *111*, 1.
[19] A. S. Mishchenko, N. Nagaosa, *Phys. Rev. Lett.* **2004**, *93*, 1.
[20] X. Liu, T. Galfsky, Z. Sun, F. Xia, E. C. Lin, Y. H. Lee, S. Kéna-Cohen, V. M. Menon, *Nat. Photonics* **2014**, *9*, 30.
[21] R. F. Ribeiro, L. A. Martínez-Martínez, M. Du, J. Campos-Gonzalez-Angulo, J. Yuen-Zhou, *Chem. Sci.* **2018**, *9*, 6325.
[22] V. A. Shahnazaryan, V. A. Saroka, I. A. Shelykh, W. L. Barnes, M. E. Portnoi, *ACS Photonics* **2019**, *6*, 904.

[23] E. Cohen-Hoshen, G. W. Bryant, I. Pinkas, J. Sperling, I. Bar-Joseph, *Nano Lett.* **2012**, *12*, 4260.
[24] G. Khitrova, A. Scherer, C. Ell, H. M. Gibbs, J. Hendrickson, T. Yoshie, O. B. Shchekin, D. G. Deppe, G. Rupper, *Nature* **2004**, *432*, 200.
[25] A. Laucht, F. Hofbauer, N. Hauke, J. Angele, S. Stobbe, M. Kaniber, G. Böhm, P. Lodahl, M. C. Amann, J. J. Finley, *New J. Phys.* **2009**, *11*, DOI: 10.1088/1367-2630/11/2/023034.
[26] I. J. Luxmoore, R. Toro, O. Del Pozo-Zamudio, N. A. Wasley, E. A. Chekhovich, A. M. Sanchez, R. Beanland, A. M. Fox, M. S. Skolnick, H. Y. Liu, A. I. Tartakovskii, *Sci. Rep.* **2013**, *3*, 20.
[27] M. Cai, O. Painter, K. J. Vahala, **2000**, 3.
[28] J. Dintinger, S. Klein, F. Bustos, W. L. Barnes, T. W. Ebbesen, **2005**, 1.
[29] B. J. Dintinger, S. Klein, T. W. Ebbesen, **2006**, 1267.
[30] Y. Sugawara, T. A. Kelf, J. J. Baumberg, **2006**, *266808*, 1.
[31] G. A. Wurtz, P. R. Evans, W. Hendren, R. Atkinson, W. Dickson, R. J. Pollard, A. V Zayats, W. Harrison, C. Bower, **2007**, DOI: 10.1021/nl070284m.
[32] J. Bellessa, C. Symonds, K. Vynck, A. Lemaitre, A. Brioude, L. Beaur, J. C. Plenet, P. Viste, D. Felbacq, E. Cambril, P. Valvin, **2009**, *2*, 2.
[33] I. Pockrand, J. D. Swalen, R. Santo, A. Brillante, M. R. Philpott, I. Pockrand, J. D. Swalen, R. Santo, A. Brillante, M. R. Philpott, **2010**, *4001*, DOI: 10.1063/1.437121.
[34] R. J. Moerland, H. T. Rekola, **2014**, DOI: 10.1021/nl4035219.
[35] T. K. Hakala, J. J. Toppari, A. Kuzyk, M. Pettersson, H. Tikkanen, H. Kunttu, P. To, **2009**, *053602*, 1.
[36] K. C. Vernon, P. Mulvaney, T. J. Davis, **2010**, 274.
[37] D. E. Gómez, K. C. Vernon, P. Mulvaney, T. J. Davis, D. E. Gómez, K. C. Vernon, P. Mulvaney, T. J. Davis, **2012**, *073108*, DOI: 10.1063/1.3313935.
[38] K. F. Mak, J. Shan, *Nat. Photonics* **2016**, *10*, 216.
[39] X. Duan, C. Wang, A. Pan, R. Yu, X. Duan, *Chem. Soc. Rev.* **2015**, *44*, 8859.
[40] M. E. Kleemann, R. Chikkaraddy, E. M. Alexeev, D. Kos, C. Carnegie, W. Deacon, A. C. De Pury, C. Große, B. De Nijs, J. Mertens, A. I. Tartakovskii, J. J. Baumberg, *Nat. Commun.* **2017**, *8*, DOI: 10.1038/s41467-017-01398-3.
[41] J. Wen, H. Wang, W. Wang, Z. Deng, C. Zhuang, Y. Zhang, F. Liu, J. She, J. Chen, H. Chen, S. Deng, N. Xu, *Nano Lett.* **2017**, *17*, 4689.
[42] S. Lepeshov, M. Wang, A. Krasnok, O. Kotov, T. Zhang, H. Liu, T. Jiang, B. Korgel, M. Terrones, Y. Zheng, A. Alú, *ACS Appl. Mater. Interfaces* **2018**, *10*, 16690.
[43] M. Stührenberg, B. Munkhbat, D. G. Baranov, J. Cuadra, A. B. Yankovich, T. J. Antosiewicz, E. Olsson, T. Shegai, *Nano Lett.* **2018**, *18*, 5938.
[44] M. Geisler, X. Cui, J. Wang, T. Rindzevicius, L. Gammelgaard, B. S. Jessen, P. A. D. Gonçalves, F. Todisco, P. Bøggild, A. Boisen, M. Wubs, N. A. Mortensen, S. Xiao, N. Stenger, *ACS Photonics* **2019**, *6*, 994.
[45] W. Liu, B. Lee, C. H. Naylor, H. S. Ee, J. Park, A. T. C. Johnson, R. Agarwal, *Nano Lett.* **2016**, *16*, 1262.
[46] Z. Li, Y. Li, T. Han, X. Wang, Y. Yu, B. Tay, Z. Liu, Z. Fang, *ACS Nano* **2017**, *11*, 1165.
[47] S. Zu, B. Li, Y. Gong, Z. Li, P. M. Ajayan, Z. Fang, *Adv. Opt. Mater.* **2016**, *4*, 1463.
[48] S. Wang, S. Li, T. Chervy, A. Shalabney, S. Azzini, E. Orgiu, J. A. Hutchison, C. Genet, P. Samorì, T. W. Ebbesen, *Nano Lett.* **2016**, *16*, 4368.
[49] A. Kinkhabwala, Z. Yu, S. Fan, Y. Avlasevich, K. Müllen, W. E. Moerner, *Nat. Photonics* **2009**, *3*, 654.
[50] K. Santhosh, O. Bitton, L. Chuntonov, G. Haran, *Nat. Commun.* **2016**, *7*, 1.
[51] R. Q. Li, D. Hernángomez-Pérez, F. J. García-Vidal, A. I. Fernández-Domínguez, *Phys. Rev. Lett.* **2016**, *117*, 1.
[52] S. J. D. Phoenix, P. L. Knight, *Phys. Rev. A* **1991**, *44*, 6023.
[53] B. W. Shore, P. L. Knight, *J. Mod. Opt.* **1993**, *40*, 1195.
[54] G. Zengin, M. Wersäll, S. Nilsson, T. J. Antosiewicz, M. Käll, T. Shegai, **2015**, *157401*, 1.
[55] R. Liu, Z. K. Zhou, Y. C. Yu, T. Zhang, H. Wang, G. Liu, Y. Wei, H. Chen, X. H. Wang, *Phys. Rev. Lett.* **2017**, *118*, 1.
[56] S. R.-K. Rodriguez, *Eur. J. Phys.* **2016**, *37*, 025802.
[57] Y. Ding, Y. Wang, J. Ni, L. Shi, S. Shi, W. Tang, *Phys. B Condens. Matter* **2011**, *406*, 2254.
[58] H. Zeng, G. Liu, J. Dai, Y. Yan, B. Zhu, R. He, L. Xie, S. Xu, **2013**, 2.
[59] R. Esteban, J. Aizpurua, G. W. Bryant, *New J. Phys.* **2014**, *16*, 013052.
[60] B. Lee, J. Park, G. H. Han, H. Ee, C. H. Naylor, W. Liu, A. T. C. Johnson, R. Agarwal, **2015**, DOI: 10.1021/acs.nanolett.5b01563.
[61] A. Darweesh, S. Bauman, D. Debu, J. Herzog, *Nanomaterials* **2018**, *8*, 809.
[62] M. Wersä, J. Cuadra, T. J. Antosiewicz, S. Balci, T. Shegai, M. Wersäll, J. Cuadra, T. J. Antosiewicz, S. Balci, T. Shegai, *Nano Lett.* **2017**, *17*, 551.

[63] X. Liu, T. Galfsky, Z. Sun, F. Xia, E. Lin, Y.-H. Lee, S. Kéna-Cohen, V. M. Menon, *Nat. Photonics* **2015**, *9*, 30.
[64] Y. Li, A. Chernikov, X. Zhang, A. Rigosi, H. M. Hill, A. M. Van Der Zande, D. A. Chenet, E. Shih, J. Hone, T. F. Heinz, **2014**, *205422*, 1.
[65] A. Laturia, M. L. Van de Put, W. G. Vandenberghe, *npj 2D Mater. Appl.* **2018**, *2*, 1.

Acknowledgements

This work is supported in part by Singapore Ministry of Education Academic Research Fund TIER 1 under Grant No. 2017-T1-001-239 (RG91/17 (S)), TIER 2 under Grant No. MOE2015-T2-1-145, A*Star AME programmatic grant under grant no. A18A7b0058, A*Star (SERC 1720700038 and SERC A1883c0002), the Ministry of Education (RG177/17) Singapore, MOE2016-T2-2-159, MOE2016-T2-1-128, National Research Foundation, and Competitive Research Program (NRF-CRP18-2017-02), and the Spanish MINECO under contracts MAT2014-53432-C5-5-R and FIS2015-64951-R.

Author contributions

YL, DHZ, QJW supervised the project. YL and FJGV conceived the idea, while LL, LYMT designed the experiments. LL characterized the bright-field and dark-field responses of the WS_2-nanoantenna systems, and performed the numerical analysis. LYMT fabricated the gold bowtie and square dimer antenna arrays with sub-10 nm gaps, and performed data analysis. LL performed the photoluminescence and Raman scattering measurements of the CVD-grown and mechanically exfoliated WS_2. JT performed atomic layer deposition of Al_2O_3, while XY mechanically exfoliated and transferred monolayer WS_2 on the sample. BQ fabricated and performed SEM inspection of gold nanoantenna arrays coupled with exfoliated WS_2. LL and LYMT write the manuscript with the inputs from all authors. LL and LYMT contributed equally. All authors discussed the results and commented on the manuscript.

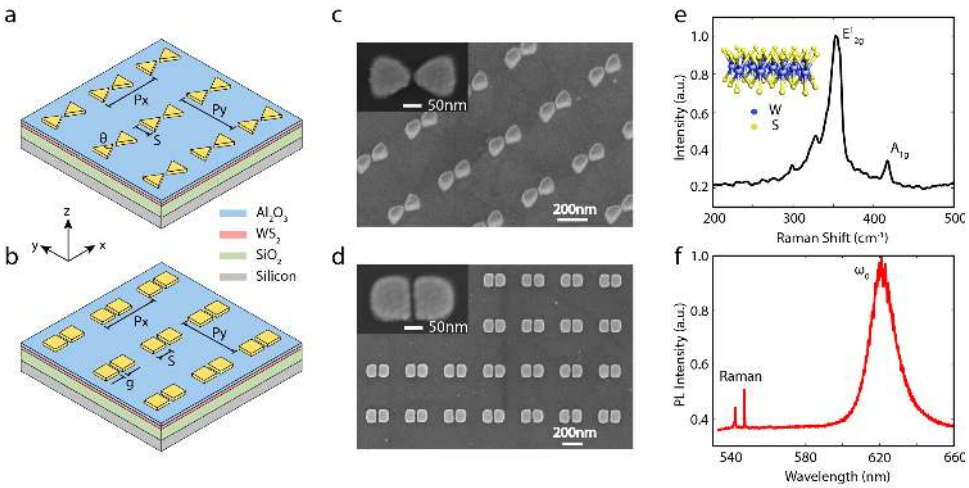

Figure 1. Hybrid TMDC-nanoantenna array systems. (a)-(b) Schematics of gold bowtie and square dimer arrays coupled with monolayer WS_2 separated by dielectric spacer layer. (c)-(d) Scanning electron micrographs of the fabricated gold nanoantenna with sub-10 nm gaps. (e) Raman spectrum and (f) photoluminescence of monolayer WS_2.

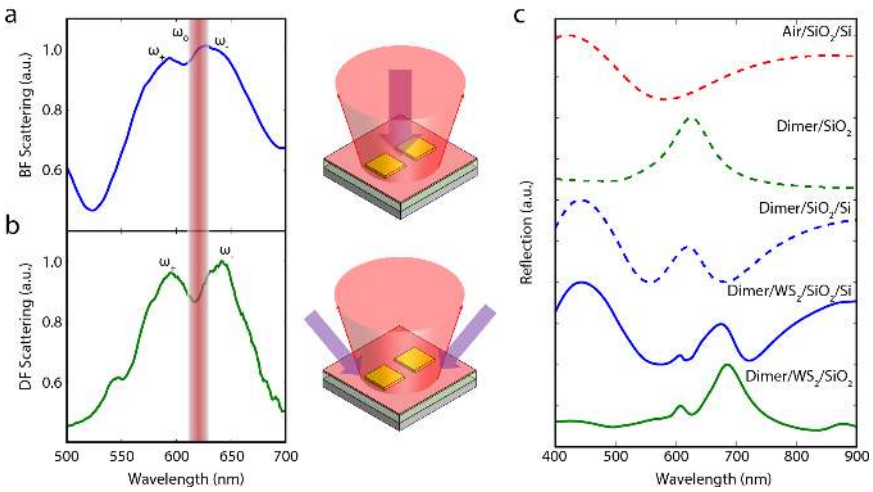

Figure 2. Resonance splitting near zero detuning for gold square dimer coupled with monolayer WS_2. (a) Bright-field and (b) Dark-field optical responses of square dimers with nominal side length $s = 60nm$ and gap spacing $g = 20nm$. The optical response of monolayer WS_2 exciton ($\omega_0 = 2$ eV) is denoted by the red band whose width represents the emission linewidth ($\gamma_0 = 64$ meV). (c) Fullwave simulations depicting mode interference between LSP resonance of gold nanoantenna and FP resonance of multiple thin film reflections.

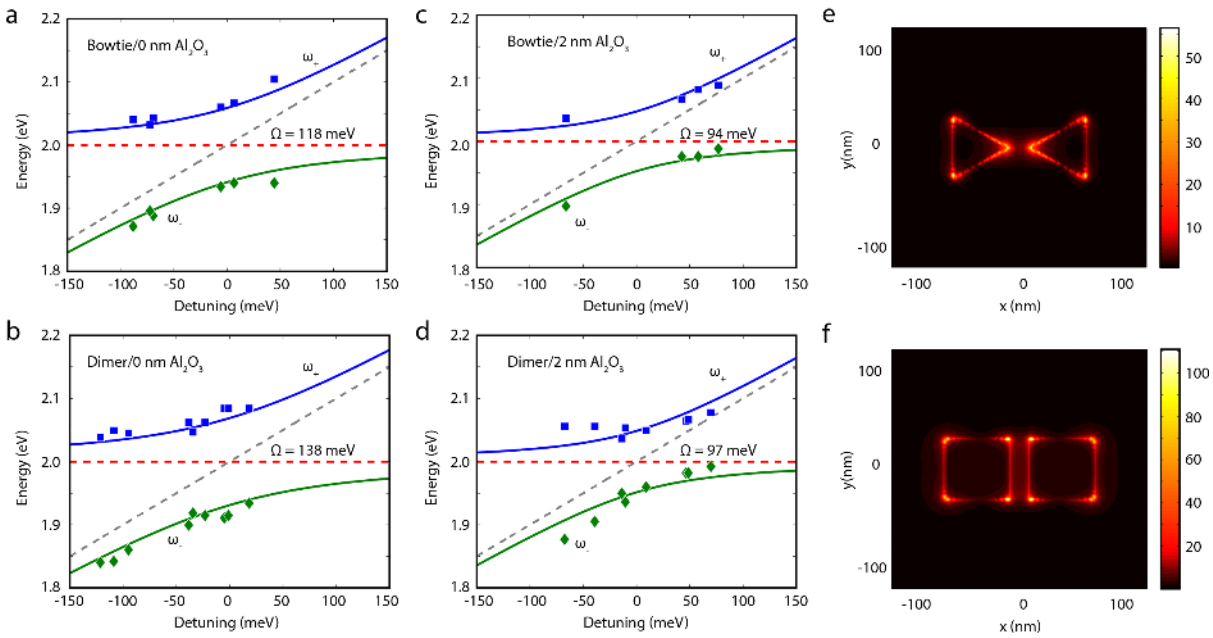

Figure 3. Anti-crossing behaviors in strongly coupled systems for (a) bowtie and (b) square dimer antennae. The effect of 2 nm thick Al_2O_3 spacer in reducing spatial mode overlap is demonstrated in (c) for bowtie and (d) for square dimer. Corresponding $|E|$-field distributions at near zero detuning for (e) bowtie ($s = 60nm, \theta = 60°$) and (f) square dimer ($s = 60nm, g = 20nm$) arrays.

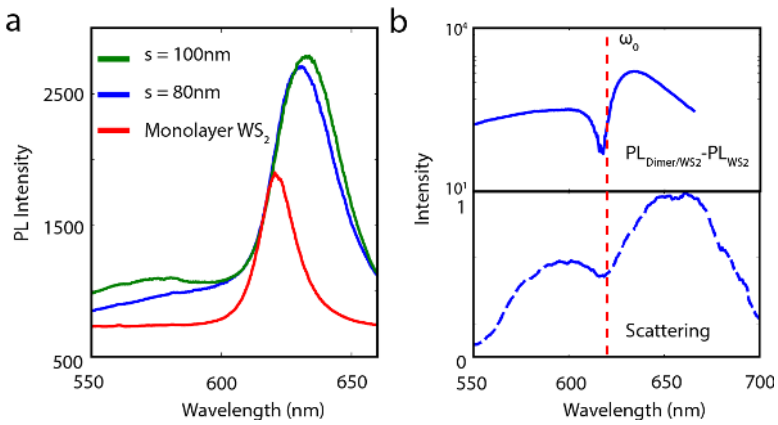

Figure 4. Photoluminescence of WS_2-dimer system. (a) PL responses of uncoupled monolayer WS_2 on SiO_2/Si substrate (red curve), and monolayer WS_2 coupled with square dimers with s = 80 nm, g = 30 nm (blue curve) and s = 100 nm, g = 30 nm (green curve). (b) The PL response of the dimer structure in log-scale, in comparison with the dark fields scattering response of square dimer with s = 80 nm, g = 30 nm.

Supporting Information

Strong Plasmon-Exciton Interactions on Nanoantenna Array-Monolayer WS_2 Hybrid System

Lin Liu[1,ǂ], Landobasa Y.M. Tobing[1,ǂ], Xuechao Yu[1], Jinchao Tong[1], Bo Qiang[1], Francisco J. Garcia-Vidal[2,3], Dao Hua Zhang[1,*], Qi Jie Wang[1,*], and Yu Luo[1,*]

[1]School of Electrical & Electronic Engineering, Nanyang Technological University, Singapore, 639798.

[2]Departamento de Física Teorica de la Materia Condensada and Condensed Matter Physics Center (IFIMAC), Universidad´ Autonoma de Madrid, 28049 Madrid, Spain.

[3]Donostia International Physics Center (DIPC), Donostia/San Sebastian, Spain.

[ǂ]These authors contributed equally to this work.
[*]Correspondence should be addressed to YL (luoyu@ntu.edu.sg), QJW (qjwang@ntu.edu.sg) , DHZ (edhzhang@ntu.edu.sg).

1. Spectral mapping measurement setup

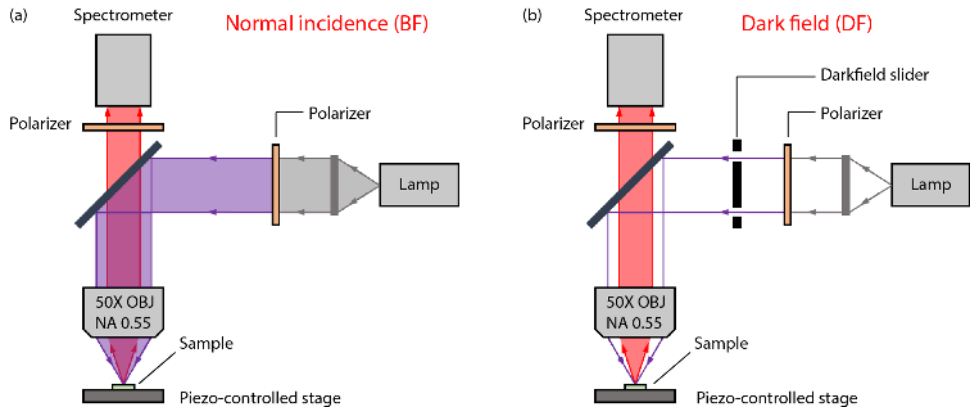

Figure S1. Spectral mapping measurement setup based on (a) bright-field (BF) and (b) dark-field (DF) geometries.

2. Design of bowtie and square dimer antennae with near zero detuning

We designed gold bowtie and square dimer antenna arrays with their LSP resonances close to the WS_2 exciton (at 620 nm), as presented in Table S1. The resonance Q factor is defined as $Q = \lambda_R/\Delta\lambda_{fwhm}$, while the mode area ($A_{\text{eff}}$) is calculated by

$$A_{\text{eff}} = \frac{1}{max[W(r)]}\int_{A_\infty} W(r)dA, \tag{S1}$$

where $W(r)$ is the electromagnetic energy density defined as

$$W(r) = \frac{1}{2}Re\left\{\frac{d[\omega\epsilon(r)]}{d\omega}\right\}\left|\vec{E}(r)\right|^2 + \frac{1}{2}\mu_0\left|\vec{H}(r)\right|^2. \tag{S2}$$

Based on our numerical simulations, bowtie is shown to have smaller mode area than square dimer, as expected from its intense field localization at the tips. However, we also found that its Q factor is lower than the square dimer. In the perspective of Q/V, which is essential for antenna-emitter coupling, square dimer is more preferable

as it exhibits higher Q/V than bowtie antenna. This is later verified experimentally, where wider Rabi splitting is observed for gold square dimer arrays.

Table S1. Designs and parameters of bowtie and square dimer nanoantenna arrays.

	Bowtie	**Dimer**
Geometry	$s = 60\ nm$ $\theta = 60°$ $P_{x,y} = 4s$	$s = 60\ nm$ $g = 20\ nm$ $P_{x,y} = 4s$
λ_R	$617\ nm$	$623\ nm$
Q	4.7	7.9
A_{eff}	$166.2\ nm^2$	$209\ nm^2$

3. Geometrical tuning of LSP resonance of gold square dimers

We fabricated gold square dimer arrays with slightly conductive ITO-coated glass based on the same nanofabrication process. The LSP resonances of these dimers are characterized more precisely by transmission measurements. As shown in Fig. S2a-b, we demonstrate that LSP resonance can be largely tuned by adjusting the side length (Fig. S2a) and gap spacing (Fig. S2b) of the square dimers. Specifically, we show that the uncoupled square dimer with nominal s = 60 nm, g = 20 nm exhibit LSP resonance very close to the WS_2 exciton (Fig. S2b). For such near zero detuning structure, we characterize its resonance wavelength (λ_R), linewidth ($\Delta\lambda_{fwhm}$), and Q-factor (Q) as $\lambda_R = 620\ nm\ (2eV)$, $\Delta\lambda_{fwhm} = 77nm\ (247.8meV)$, $Q = 8$. These experimental values agree with our numerical simulations in Table. S1. In Fig. S2c, we present the experimental dark field scattering of the near zero detuning gold square dimer in the presence of 2 nm thick Al_2O_3 interlayer.

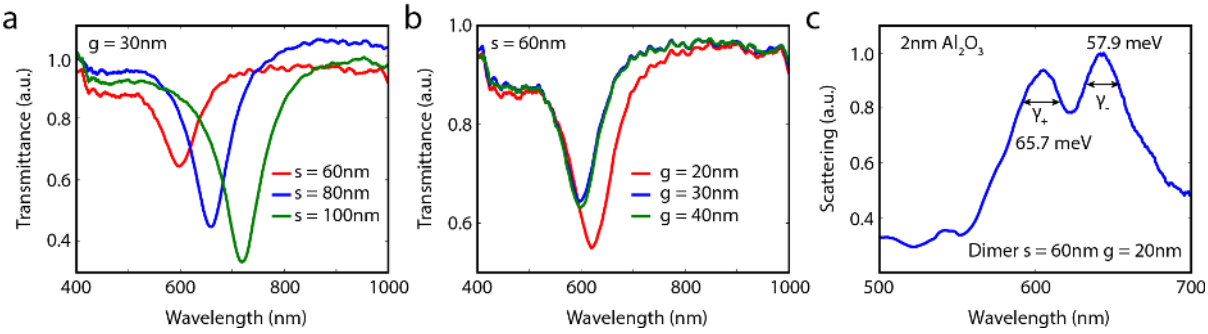

Figure S2. Transmittance of square dimer nanoantennae on ITO substrate based on different (a) nominal side lengths (at fixed nominal gap of 30 nm), and (b) gap sizes (for a fixed nominal side length of 60 nm). (c) Experimental dark field scattering of square dimers ($s = 60nm$, $g = 20nm$) coupled with monolayer WS_2, in the presence of 2nm Al_2O_3 spacer layer.

4. Anti-crossing behaviors of array and isolated gold dimer structures

Rabi splitting for square dimer nanoantenna arrays coupled with monolayer WS_2 is larger than that from single nanoantenna hybrid system. The red dashed line represents exciton energy level. Here in Fig. S3a and S3b, the red lines are not at the same level. The energy level shift comes from different binding energy of monolayer WS_2 with different substrate. But the monolayer property has still maintained. Compared from Fig. S3(c) and S3(d), the e-field enhancement for periodic nanoantenna is near 2.5x higher.

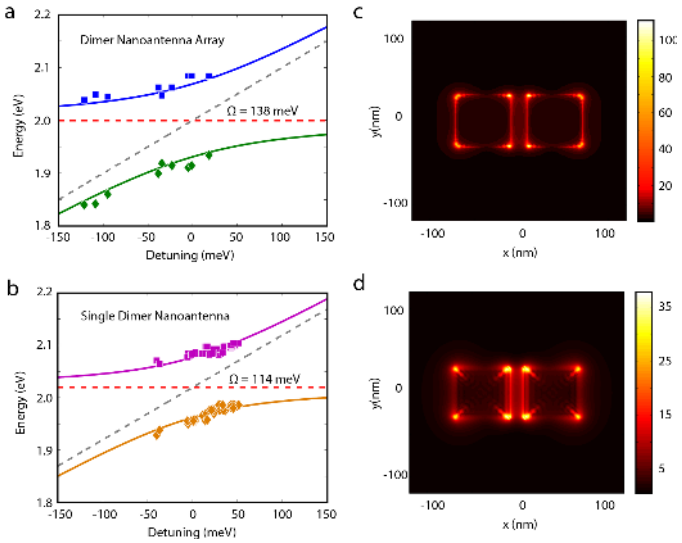

Figure S3. Compare of dimer nanoantenna arrays with single dimer nanoantenna coupled system. (a)(b) Anti-crossing spectra. E-field distribution for (c) dimer nanoantenna arrays and (d) single dimer nanoantenna with $s = 60\text{nm}, g = 20\text{nm}$.

The schematic of dimer nanoantenna with 20nm gap (a) without and (c) with 2nm spacer are shown in Fig. S4. Corresponding E-filed distribution are presented in (b) and (d). Plasmons are confined in the ultrathin dielectric layer, leading to decrease of spatial overlap. A decrease in the coupling strength is formed.

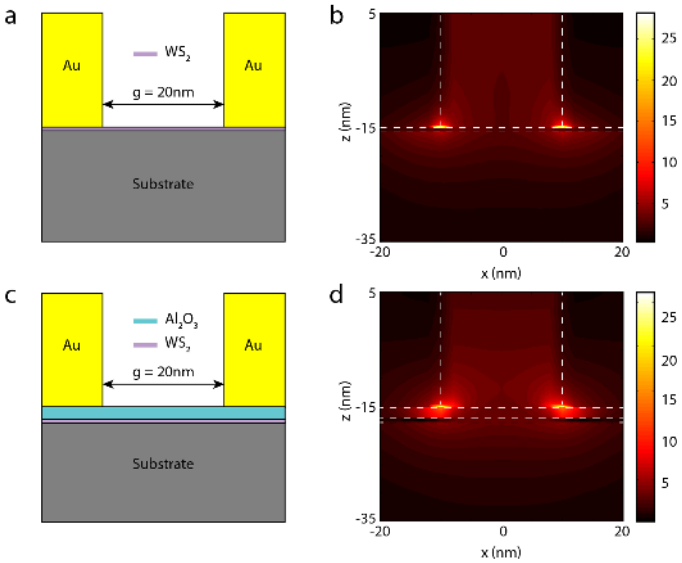

Figure S4. Side view of E-field distribution in xz-plane for coupled system (a)(b) without spacer layer, (c)(d) with 2nm Al_2O_3 spacer.

5. Photoluminescence of mechanically exfoliated monolayer WS_2 coupled with gold dimers

A side shoulder in PL spectrum of the hybrid system has been observed. With the change of geometry of square dimer nanoantennae, the main peak and side shoulder can be tuned.

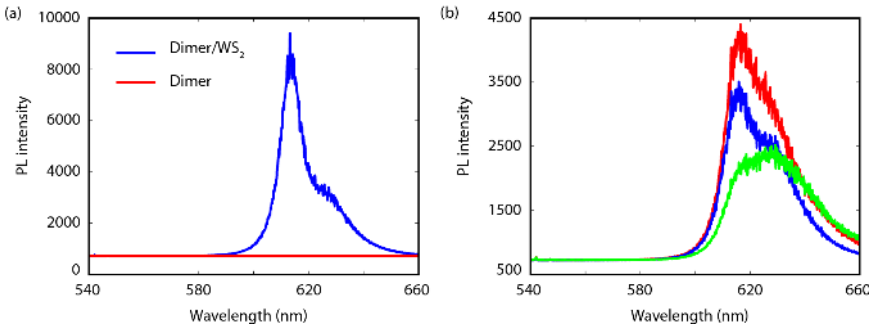

Figure S5. PL of square dimer nanoantennae-WS_2 hybrid system from a new fabricated sample. (a) Compare PL from hybrid system with bare nanoantenna arrays. (b) PL from different geometry square dimer nanoantennae hybrid system.

6. Scattering cross section and absorption cross section of monolayer WS_2 coupled with gold dimers

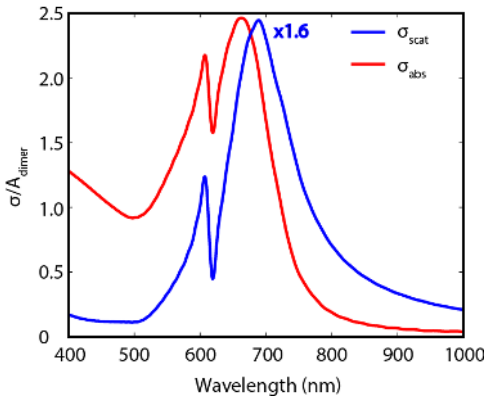

Figure S6. Scattering (blue) and absorption (red) cross sections normalized by the square dimer nanoantenna geometrical area (side length $s = 60nm$ and gap spacing $g = 20nm$). The scattering cross section has been multiplied by 1.6 to match the scale.

The splitting of absorption cross section is narrower compared with the splitting of scattering cross section, which is the leading cause of narrower splitting in PL spectrum compared with that in DF scattering spectrum.